Journal of Power Sources 195 (2010) 3553–3568

Contents lists available at ScienceDirect

Journal of Power Sources

journal homepage: www.elsevier.com/locate/jpowsour

In situ comparison of water content and dynamics in parallel, single-serpentine, and interdigitated flow fields of polymer electrolyte membrane fuel cells

Dusan Spernjak, Ajay K. Prasad*, Suresh G. Advani

Center for Fuel Cell Research, Department of Mechanical Engineering, University of Delaware, 126 Spencer Lab, Newark, DE 19716, United States

ARTICLE INFO

Article history:
Received 14 October 2009
Received in revised form 7 December 2009
Accepted 8 December 2009
Available online 16 December 2009

Keywords:
PEM fuel cell
Water transport
Flow field configuration
Neutron imaging
Optical imaging
Anode flooding

ABSTRACT

Water content and dynamics were characterized and compared in situ by simultaneous neutron and optical imaging for three PEM fuel cell flow fields: parallel, serpentine, and interdigitated. Two independent sets of images were obtained simultaneously: liquid water dynamics in the flow field (channels and manifolds) were recorded by a digital camera through an optical window, while the through-thickness integrated water content was measured across the cell area by neutron imaging. Complementary data from the concurrent images allowed distinguishing between the water dynamics on the cathode and the anode side. The transient water content within the cell measured using neutron imaging is correlated with optical data as well as with temporal variations in the cell output and pressure differentials across the flow fields. Water dynamics on both the cathode and anode side were visualized and discussed.

The serpentine cell showed stable output across the current range and the highest limiting current. Parallel and interdigitated cells exhibited substantially higher water contents and lower pressure differentials than the serpentine. Anode flooding significantly impeded their performance at high current. At moderate current, cell output correlated with the changes in water distribution in the cathode flow field rather than with the variations in the overall water content. Performance of the interdigitated cell was similar to the serpentine one in spite of the vastly different water contents.

The cell's water-content response to a step-change in current revealed three distinct stages of water accumulation. Flow field configuration greatly affected both the amount of water accumulated in the cell and the duration of each stage.

1. Introduction

Bipolar plates (or, the flow-field plates) are among the key components of a polymer electrolyte membrane (PEM) fuel cell (Fig. 1). Their most important functions are to distribute reactant gases through the channels, transport electrons through the lands, and remove excess heat and water from the electrodes and out of the cell [1–3]. In addition, the bipolar plates provide structural support for the system, separate the anode and cathode gases in a fuel cell stack, and provide the means for heat management (and in the case of porous plates, additional water management [4,5]).

PEM fuel cell operation requires water management throughout the cell, i.e. maintaining a sufficient level of membrane hydration (to ensure protonic conductivity) while removing the excess water (to admit fresh reactant gases to the catalyst layers). Flow field design [3,6–8] strongly affects the gas and water transport in PEM fuel cells, and hence the cells' performance, dynamic response, and durability. However, a complete understanding of the relationships between the water content, distribution, and dynamics and the cell performance and durability has not yet been realized.

Various experimental techniques have emerged in an attempt to visualize and quantify the water transport in operating PEM fuel cells [9,10]. Optical imaging has been used extensively due to its flexibility regarding the spatial and temporal resolutions [11–16]. The technique allows imaging the water dynamics only in the flow channels (Figs. 1 and 2), since the pores of the gas diffusion layer (GDL) are not optically accessible. Hence, water becomes visible only after it emerges from the GDL/channel interface, where it forms droplets initially adhering to the GDL. Unless detached from the GDL surface, a droplet may continue to grow until it eventually fills the entire channel cross-section and blocks the flow in the channel. Such a situation of complete channel blockage was encountered in parallel flow fields [11,15], causing a sharp prolonged drop in the cell output, accompanied by an increased pressure differential across the flow field. Different amounts of localized water may clog the channel, such as a thick continuous slug [15] or a thin film of water (i.e. a sealed water band) [11].

Hence, to prevent extended channel clogging, excess water needs to be efficiently and continuously transported both (i)

* Corresponding author. Tel.: +1 302 831 2960; fax: +1 302 831 3619.
E-mail addresses: spernjak@udel.edu (D. Spernjak), prasad@udel.edu (A.K. Prasad), advani@udel.edu (S.G. Advani).

0378-7753/$ – see front matter © 2009 Elsevier B.V. All rights reserved.
doi:10.1016/j.jpowsour.2009.12.031

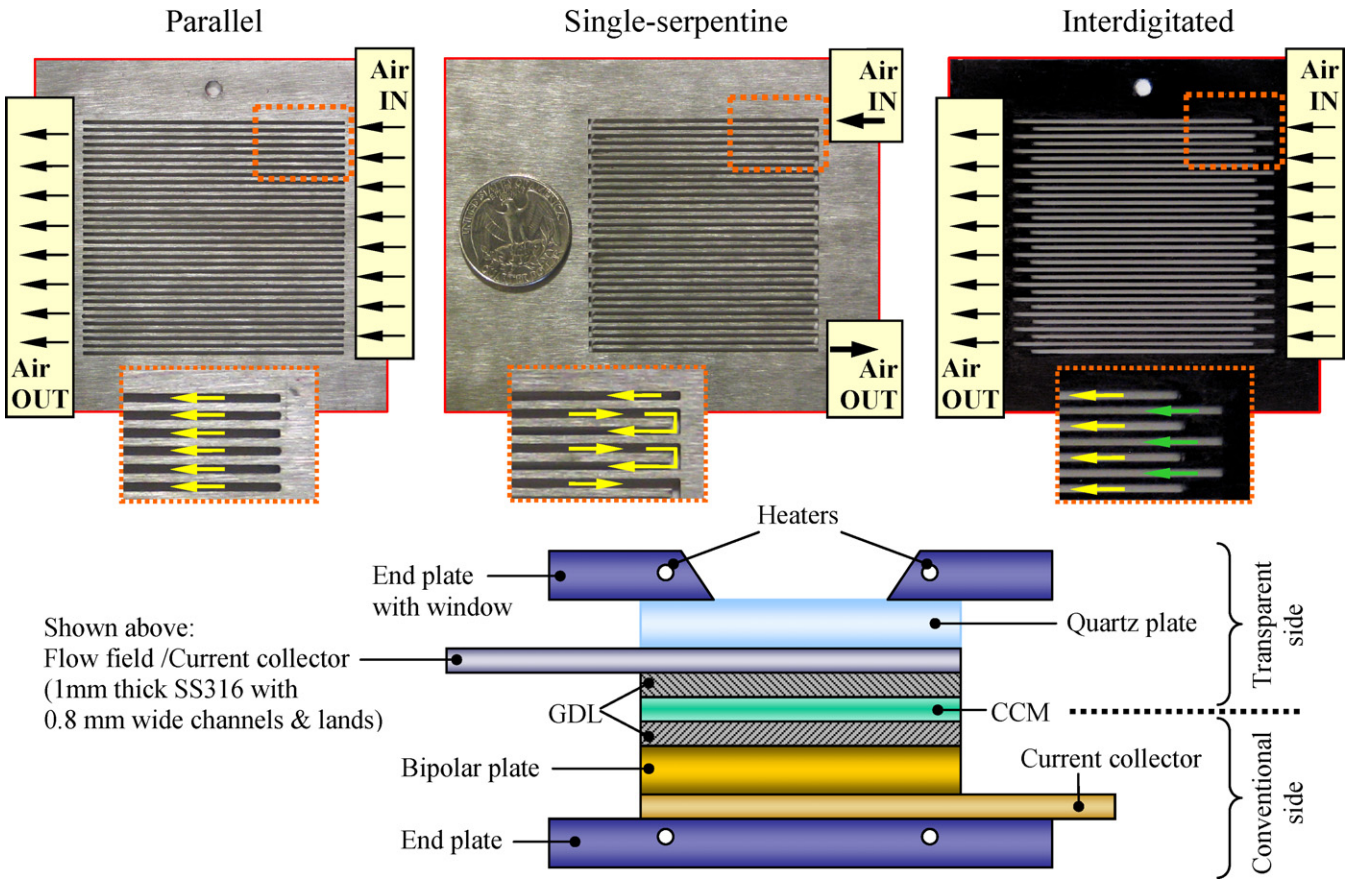

Fig. 1. Schematic of the operational PEM fuel cell with visually accessible channels.

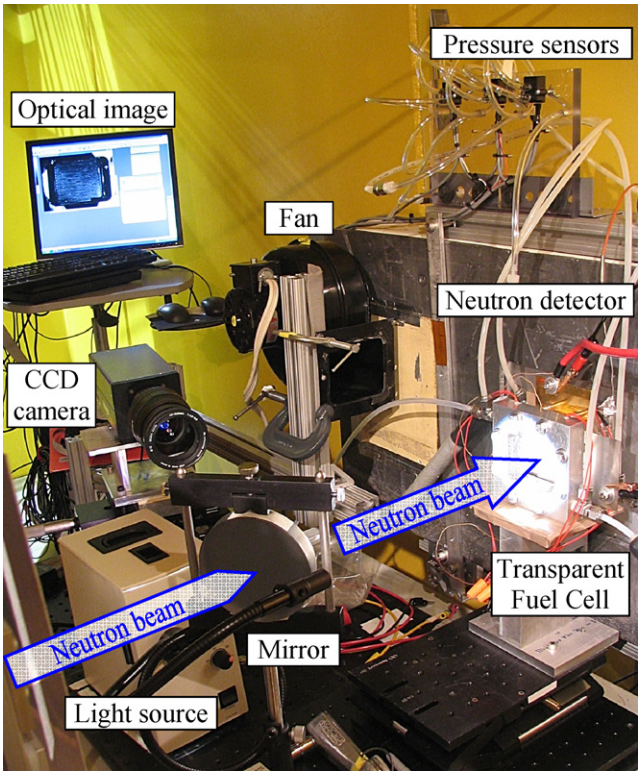

Fig. 2. Experimental setup for simultaneous neutron and optical imaging at NIST Center for Neutron Research.

through the GDL into the flow field and (ii) along the flow channels out of the cell. Transport in the channels is initiated by the droplet's detachment from the GDL surface. Critical droplet size (i.e. detachment diameter) may be predicted from the balance of drag force and surface adhesion force [16–21]. The major limitation of optical imaging is that the top channel view generally does not allow the liquid water content to be quantified (except in special situations such as when the droplets do not interact with the channel walls). On the other hand, neutron imaging enables measuring the water content (i.e. thickness) across the cell area. The technique has therefore been widely used to study water transport in operating fuel cells despite the limited availability of neutron-imaging facilities [14,22–31].

Kramer et al. [22] compared water distribution in a 50-channel interdigitated and a 10-pass serpentine flow fields. In the serpentine flow field, mass transport was limited by GDL flooding although the water was efficiently removed from the channels. In contrast, the interdigitated cell had much lower water content in the GDL (due to convective transport under the lands), but suffered from excessive channel flooding at 0.4 A cm^{-2} which was caused primarily by gravity (as the channels were vertical).

Hickner et al. [26] studied the cell's transient response to a step-change in current. It was shown that the response in the water content lags behind the current density step, which was attributed to the characteristic time for capillary transport through the GDL. Second, both the lag time and the steady-state water content were significantly reduced as the cell operating temperature was increased. The results suggest this was caused by evaporation of water due to the local heat release from the cell reaction.

Trabold et al. [27] reported that the total water content (at constant current) did not change significantly when the cathode

stoichiometry was increased from 1.3 to 2.0. Since the water in the cathode channel would be removed more efficiently at higher air flow, it was suggested that liquid water may have existed in the anode channel. In a subsequent study [32], distinguishing between liquid water in the cathode and anode flow fields was made possible by rotating the anode and cathode channels in plane by 90° (making them orthogonal). Stagnant pools of water were observed in the anode channels throughout the tests, albeit without a notable effect on the performance.

A similar approach was used by [29], where parallel anode channels were oriented perpendicularly to a 5-pass serpentine on the cathode. Special masking and image processing were used to separate the water information in the anode and cathode channels. Reduction in the cell output was associated with anode channels being clogged by liquid water. Turhan et al. [25] separated the water content under the lands from the channel area, and calculated the effective porosity based on the saturation level of the cathode GDL obtained from neutron data. Negative values for the effective porosity under the lands indicated that the anode GDL was also flooded. More recently, development of high-resolution imaging enabled measuring cross-sectional water profiles [30,31], again indicating anode flooding. Finally, in our previous work with an optically accessible single-serpentine cell [13], water accumulation was observed at the anode serpentine U-turns. Note that the above examples all incorporate a microporous layer (MPL) on the cathode side, which is often used as a passive water management tool due to its resistance to flooding (high saturation pressure in small hydrophobic pores). Hence, when water condenses at the interface between the cathode catalyst layer and the MPL, the MPL acts like a pressure barrier forcing the water across the membrane. However, not enough attention has been devoted to characterizing anode flooding.

Because the water content is integrated along the neutron beam direction, the main issue with neutron imaging is the inability to distinguish the water location at different penetration depths (i.e. lack of depth perception). We recently demonstrated the utility of a novel experimental approach, where neutron and optical were combined and performed simultaneously in operating fuel cells [14]. Here, two sets of images were obtained concurrently in situ: liquid water dynamics in the flow field were recorded a digital camera through the optical window, while the integrated water content across the cell thickness was measured by neutron imaging. The transient behavior of water content within the cell obtained from neutron imaging is correlated with optical data as well as with temporal variations in the cell output and pressure drop across the flow fields. Such an approach provides complementary data that enables improved interpretation of the images, both optical and neutron.

In the present study, water content and dynamics were quantified and compared in fuel cells with single-serpentine, parallel, and interdigitated flow fields. Fully saturated inlet gas streams in a counter-flow arrangement minimized the issue of inadequate membrane hydration, thus underlining the differences in water removal between the flow fields. The flow fields were tested under conditions of high cathode-channel flooding, i.e. in a scenario where the GDL flooding is decreased by using wet-proofed material (proven to efficiently expel water from the catalyst layer into the channel [13]). Finally, liquid water dynamics were visualized optically in both cathode and anode flow fields.

2. Experimental setup and procedure

The experimental setup (Figs. 1 and 2) was comprised of five systems: (i) an operating PEM fuel cell with active area of 25 cm^2 (Table 1), (ii) fuel cell test station, (iii) optical imaging system, (iv) neutron imaging system, and (v) pressure measurement station. To ensure accurate time synchronization between the data sets, computers for data acquisition (fuel cell test stand, optical imaging station, neutron imaging station, pressure sensor station) were connected in a local area network (LAN) and controlled via time server (Net Time Server & Client 2.1). Below we summarize the main features pertinent to the present work, while additional details are given in [14].

Table 1
Fuel cell materials and metrics; operating conditions.

Fuel cell design	
Active area	5 by 5 cm
Channel	0.8 mm wide, 1 mm deep
Land (rib)	0.8 mm wide
Manifolds	2.5 by 2.5 mm
GDL (by SGL carbon)	
Cathode	SGL35BC (with MPL)
Anode	SGL31BA
Membrane, catalyst-coated (by Ion Power, Inc.)	Nafion-based, 25 μm thick, Pt loading 0.3 mg cm^{-2} on each side
Operating conditions	
Cell T (=dew point T) 50 °C	
Cathode (air)	
Air flow rate	1.5 or 5 slpm
Inlet air T	50 °C
Inlet RH	100%
Backpressure	100 kPa
Anode (H_2), counter-flow	
H_2 flow rate	0.5 slpm
Inlet H_2 T	50 °C
Inlet RH	100%
Backpressure	100 kPa

2.1. Fuel cell design

For this study, we designed and fabricated PEM fuel cells with three different flow field configurations: parallel, single-serpentine, and interdigitated. Two versions of the cell were tested for each flow field: conventional (non-transparent), and optical (with one side conventional, and the other transparent). For each case study, the same flow field was used on the cathode and anode side (i.e. the mirror image thereof).

Hardware for the *conventional* cell consisted of the end plates (25 mm thick Al 6061-T6), current collectors (2 mm thick gold-plated copper), and flow-field plates (12.7 mm thick gold-coated aluminum Al 6061-T6). The bipolar plates were exchangeable, while the other cell parts remained the same in all tests. The bipolar plates themselves had identical design parameters (active area, channel and land dimensions; Table 1) except for the channel layout.

One side of the *optical* cell was retained from the conventional version, while the other side had visually accessible channels (Figs. 1 and 2). View of the water dynamics in the channels was facilitated through a window in the end plate and the underlying quartz plate (12.7 mm thick fused silica). The flow field on the transparent side, also serving as a current collector, was fabricated by cutting the channels through a 1 mm thick plate made of stainless steel 316. Manifolds for parallel and interdigitated cells were cut into the quartz plate, to match the geometry of the transparent side to the conventional side.

The cell temperature was kept within ±2 °C of the set value (measured at the cathode end plate). Each end plate had a pair of 90 W, 10 cm long cartridge heaters, adjacent to the left and right edges of the cell active area. The heaters were placed outside the field of view so they would not interfere with the imaging. Pairs of heaters in the front and back end plates were controlled separately

to mitigate through-thickness variations in temperature. Each of the two thermocouples was placed in a hole in the end plate, with the tip just above the mid-top edge of the imaged area. Excess heat was removed continuously by forced convection with an oversized fan (Fig. 2).

The same membrane-electrode assemblies (MEAs) were used in all tests, and comprised of the catalyst-coated membrane (CCM) sandwiched between two GDLs (Table 1). The cathode GDL had an MPL facing the catalyst layer. MEAs were compressed between the lands to 85% of the original thickness of 0.66 mm. Accounting for the effective porosity of the GDLs, the average open-space thickness within the compressed GDLs was 0.48 mm (excluding the MPL and the CCM).

2.2. Fuel cell test station

A NIST fuel cell test stand was used to control and monitor the electronic load, flow rate, temperature, humidity, and backpressure at a sampling rate of 0.1 Hz. Operating conditions are summarized in Table 1. Tests were conducted with constant flow rates. For conversion to stoichiometry, 0.45 slpm of air and 0.19 slpm of hydrogen correspond to 1 A cm^{-2} equivalent flow rates for the cell tested. Tubing sections downstream from the test stand were additionally heated and arranged to mitigate water buildup between the test station and the cell.

2.3. Optical imaging system

A 12-bit LaVision Imager Intense camera with a 1376 by 1040 pixel array was used to record the optical images, with a field of view of approximately 7.3 cm × 5.5 cm. Water dynamics across the entire flow field were visualized, including the manifolds for parallel and interdigitated channels. Optical images were acquired at 2 Hz. The camera and optics were kept outside the path of the neutron beam by using a silver-coated quartz mirror (Fig. 2). An adjustable 150 W cold light source (Volpi Intralux 5100) with two fiber optic goosenecks was used to illuminate the field of view. Optical images are shown without any additional processing or averaging. The lands are masked in white to highlight the channels, and to enable direct reading of the water distribution under the lands when optical images are overlaid by the concurrent neutron images [14].

2.4. Neutron imaging system

The experiments were conducted at the National Institute of Standards and Technology (NIST), Center for Neutron Research (NCNR), Fig. 2 [23,24,33]. Neutron images were captured using one of two 10-bit amorphous-silicon detectors (Varian Paxscan®): one having a pixel pitch of 250 μm (used with serpentine and parallel flow fields), and the other with a pixel pitch of 127 μm (used with interdigitated cells). Neutron fluence rates for the two detectors were 2×10^7 and 3.3×10^7 cm^{-2} s^{-1}, respectively. The image acquisition rate was 7.5 Hz.

Attenuation of the neutron beam by water was approximated by the Beer–Lambert law, $I = I_0 \exp(-\mu t)$, where I_0 is the reference (dry) image, I is the attenuated (wet) image, μ is the attenuation coefficient of water, and t is the liquid water thickness. The reference image I_0 was obtained by averaging images of a dry cell at the operating temperature to account for the thermal expansion of the cell components. Temporal variations in the beam intensity during the experiments were accounted for by normalizing the density images with respect to an undisturbed image patch. The μ value of 0.291 mm^{-1} [14,27,28] was used to obtain the density images. Note that some recent neutron imaging studies [24,29] employ a higher μ value (thus effectively reducing the calculated water volume [14]), which was obtained by distancing the calibration cuvette from the neutron detector.

Processed neutron images presented in this work were obtained by averaging 150 consecutive images to increase signal-to-noise ratio, resulting in an effective frame rate of 0.05 Hz. Thus, when presenting a neutron image at time t, we refer to the image obtained by averaging consecutive images over the time period of [t − 10 s; t + 10 s]. The corresponding optical image was also taken at time t unless noted otherwise. The grayscale levels of the density images were then mapped to a color scheme to visually differentiate the water thickness across the cell. The same color scheme and thickness range (0.01–1 mm) were used in all neutron images in this paper.

The water content plotted in graphs was obtained by summing the water thickness across the cell active area, multiplied by the effective pixel area of the neutron panel detector. Note that the water content over the active area does not include the manifolds: water contents in the manifolds for the parallel and interdigitated flow fields are shown separately. Also, in the counter-flow scheme used in the fuel cell tests (Table 1), the cathode inlet manifold overlaps the anode outlet manifold. The graphs show the data from unaveraged neutron images, where the noise was filtered out with a 10-s moving average (75 consecutive images).

2.5. Pressure measurement station

Pressure differentials across the cathode and anode sides of the cells were measured by Honeywell sensors (accuracy 2% of the full range) connected to the cell's inlets and outlets. The data were recorded at 1 Hz via a National Instruments DAQ board used as an interface between the sensors and a computer with LabVIEW. The sensors for specific flow fields were arranged as follows: parallel anode – XCAL4004DN (1 kPa range), parallel cathode – ASCX01DN (7 kPa range), serpentine anode – ASCX05DN (35 kPa range), and serpentine cathode – ASCX30DN (210 kPa range). Pressure drop for the interdigitated flow field was obtained from sensors in the test stand, Noshok 615-100 (700 kPa) and 615-60 (420 kPa), with accuracy of 0.25%. The pressure data (regardless of the sensors) were plotted with a moving average corresponding to 2 min of data acquisition time.

For each flow field, data were collected for two versions of the cell: (i) conventional (non-transparent) cell and (ii) transparent cell with optically accessible cathode. The following data sets were obtained simultaneously for each test: test stand data, neutron images (containing the water content and distribution across the cell), optical images (showing the water distribution in the cathode flow fields only), and pressure differentials across the cathode and anode sides of the cell. Each test run included the cell startup (voltage cycling), polarization curves, short purging cycles, and voltage data at fixed currents. The same tests (without neutron imaging) were performed at the University of Delaware to ensure repeatability of the results. Additional runs were also performed with (iii) transparent cells with optically accessible anode side, where water dynamics in the anode channels were directly visualized. Experimental results are presented and organized in a same fashion throughout the text, with the common legend for all graphs given in Fig. 4.

3. Experimental results and discussion

The results are organized as follows. Sections 3.1 and 3.2 discuss the polarization curves, Section 3.3 shows the cell startup, and Section 3.4 examines the response after a step-change in current density.

3.1. Polarization curves: validation and comparison

Cell performance with the three flow fields is compared in Fig. 3 at two different air flow rates. In addition, for each flow field, polarization curves are shown for transparent and conventional cells, indicating very similar cell behavior and limiting currents for the two versions of the cell. Optical cells have higher ohmic losses than the conventional ones, mainly due to the lower current-collecting ability of the thin steel plates. This difference is the largest for the serpentine case, since only one end of each rib is connected to the plate base, while the ribs in the remaining two flow fields are attached at both ends to the plate base (Fig. 1).

When comparing performance of the cells with the three flow field geometries, Fig. 3 displays substantial difference in both the limiting currents and the shapes of the polarization curves. The parallel flow field gives inferior performance accompanied by unstable operation even at modest current densities. In contrast, the polarization curve for the single-serpentine yields a smooth shape throughout the wider ohmic region, reaching limiting currents about two times higher than the cell with the parallel flow field. The interdigitated cell performs similar to the serpentine one until it approaches the region of the limiting current density, where it exhibits unstable behavior similar to the one exhibited by the cell with parallel channels. Such a diverse cell output with different flow fields arises from differences in the transport of both reactants and products, governed by the flow field geometry. At fully humidified inlet flow (i.e. at conditions where membrane dehydration is unlikely to occur, while flooding is expected), we can hypothesize that the cell performance is primarily affected by water dynamics and the ability of the flow fields to expel the excess liquid water.

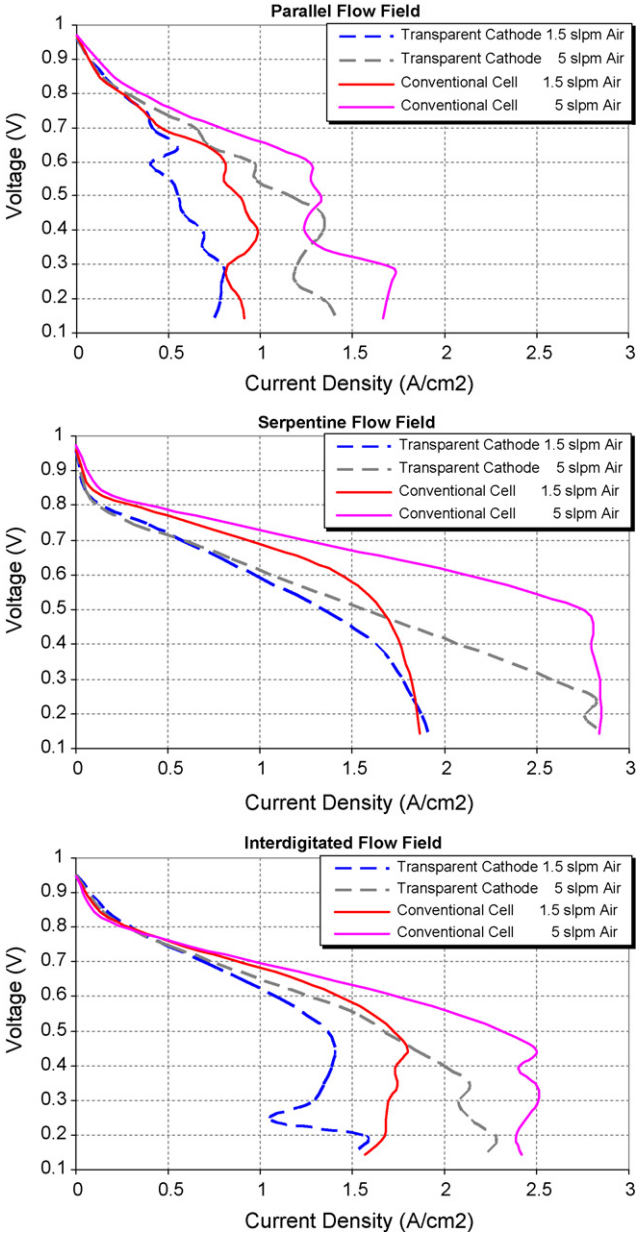

Fig. 3. PEM fuel cell performance with parallel, serpentine, and interdigitated flow fields: optical vs. conventional cells, compared at two air flow rates (1.5 and 5 slpm).

Table 2
Reynolds numbers and velocities at the channel inlet for the tests in Fig. 4 (50 °C, 100 kPa backpressure).

	Cathode		Anode	
	Re	V (m s^{-1})	*Re*	V (m s^{-1})
Parallel	57	0.58	2.7	0.195
Single-serpentine	1815	18.5	88	6.24
Interdigitated	113	1.16	5.5	0.39

In the present design (Fig. 1), the total flow in the parallel flow field is distributed between 32 channels, each 5 cm long. The serpentine flow field consists of a long continuous channel with 32 passes connected by alternating U-turns (total channel length is 1.6 m). The interdigitated cell incorporates 16 dead-ended inlet channels, separated by the adjacent lands from the 16 outlet channels. Consequently, serpentine and interdigitated cells have the inlet channel velocities and Reynolds numbers that are 32 and 2 times larger than those of the parallel individual channels, respectively. Table 2 summarizes the above statements for the test conditions depicted in Fig. 4 (while neglecting the difference in the inlet pressure).

3.2. Time evolution and water dynamics during the polarization sweep

Water dynamics hereafter will be discussed by using the data collected with the transparent cells (with the cathode side visualized). Cell performance (Fig. 3) can now be interpreted by examining the results in Figs. 4–6, where a polarization curve for each flow field is plotted vs. time, along with the water content and pressure differentials across cathode and anode sides. The polarization curves were recorded while stepping down the voltage from the open circuit to 0.15 V, with a voltage step height of 0.05 V and duration of 5 min. Water distributions during the voltage sweep at lower cathode flow rate of 1.5 slpm (Fig. 4) are depicted in the neutron images in Fig. 5. When examining the neutron images of parallel and interdigitated cells, one should keep in mind that the cathode outlet channels overlap with the anode inlet channels.

3.2.1. Parallel flow field

Parallel flow field (Fig. 4) exhibits the highest liquid water content of all three channel configurations, reaching a maximum value of 1450 mm^3 over the cell active area. Such a sluggish water removal is clearly caused by the low velocity of the main channel flow, causing the lowest pressure differential across the cell. Note that the cell already contains substantial amount of water at the start, since the short purges and open-circuit operation between the steps in the test procedure were insufficient to completely expel the water retained from the preceding step. However, this retained water did not significantly alter the limiting current, as the images and the pressure data confirm that no complete channel blockage occurred within the first 30 min of the test.

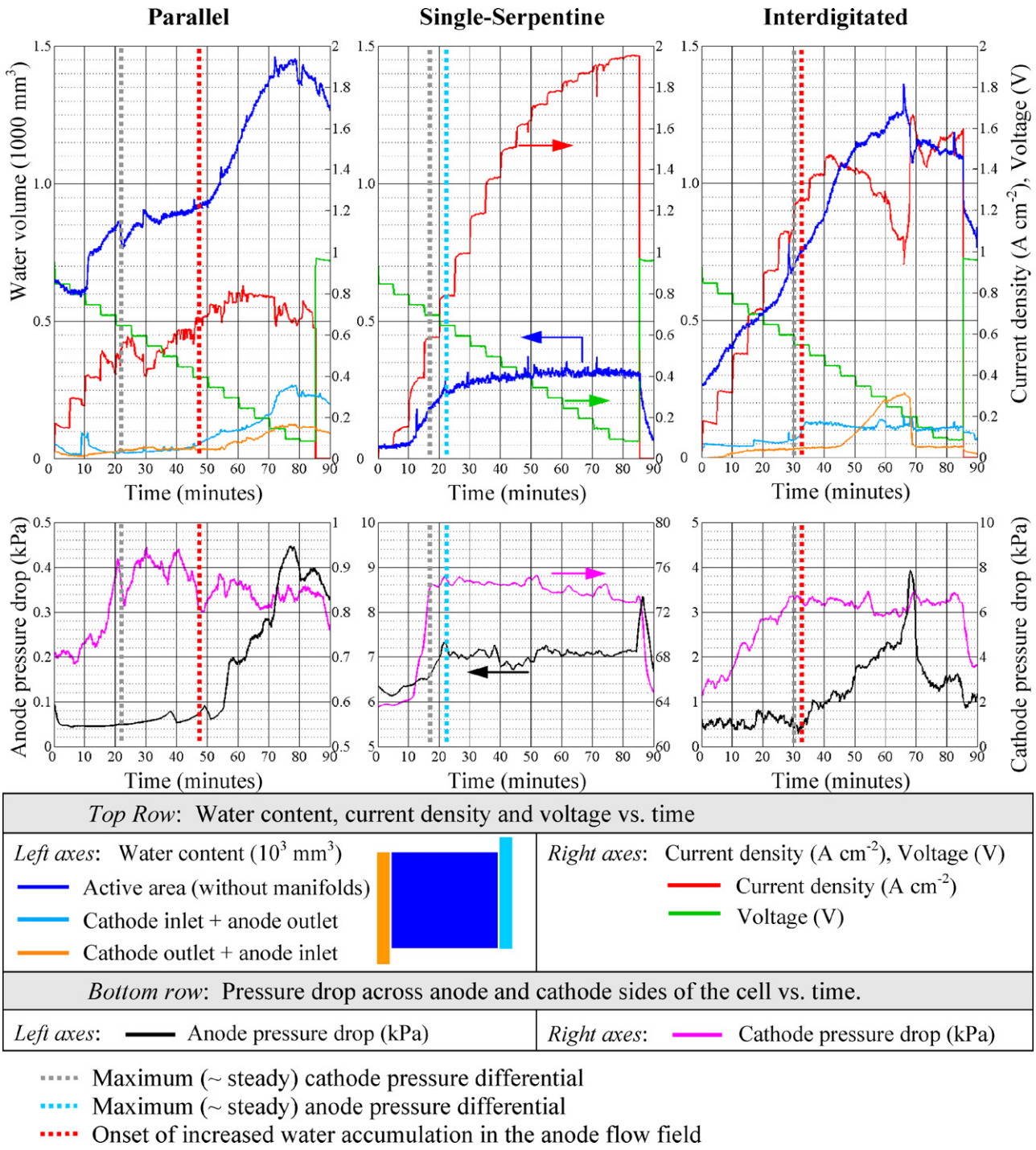

Fig. 4. Time evolution while recording the polarization curves (Fig. 3) for the cell with visualized cathode channels, with air flow rate of 1.5 slpm. Corresponding neutron images shown in Fig. 5.

In spite of the partially flooded cell, water content in the cathode channels increases notably over the first 30 min. This is evidenced by the optical images and the increase in the cathode pressure differential from 0.7 to 0.9 kPa. Droplets are dispersed randomly across the cell area, and grow while adhering to the GDL surface. Active formation of water agglomerates by the merging droplets is characteristic for the period between 30 and 40 min, causing the cathode pressure drop to level off. Thereafter, 1/3 of the channels contain stationary short slugs, while in the remaining channels water removal becomes more active. Optical images (as well as the pressure drop) show notably slower accumulation of water in the cathode flow field beyond 40 min, with repeatable water formation and removal in the active channels.

Water buildup in the anode flow field initiates during the transition phase in the cathode channels from discrete growing droplets to short slugs. Hence, it appears that the cathode is relieved from further water buildup by partially shifting the water balance to the anode side, besides the change in the water distribution in the cathode channels and active water removal therein. This is supported by the increase in the anode pressure drop by a factor of four from 50 to 70 min (0.07–0.28 kPa). This transfer in water accumulation from the cathode to the anode side is beneficial only temporar-

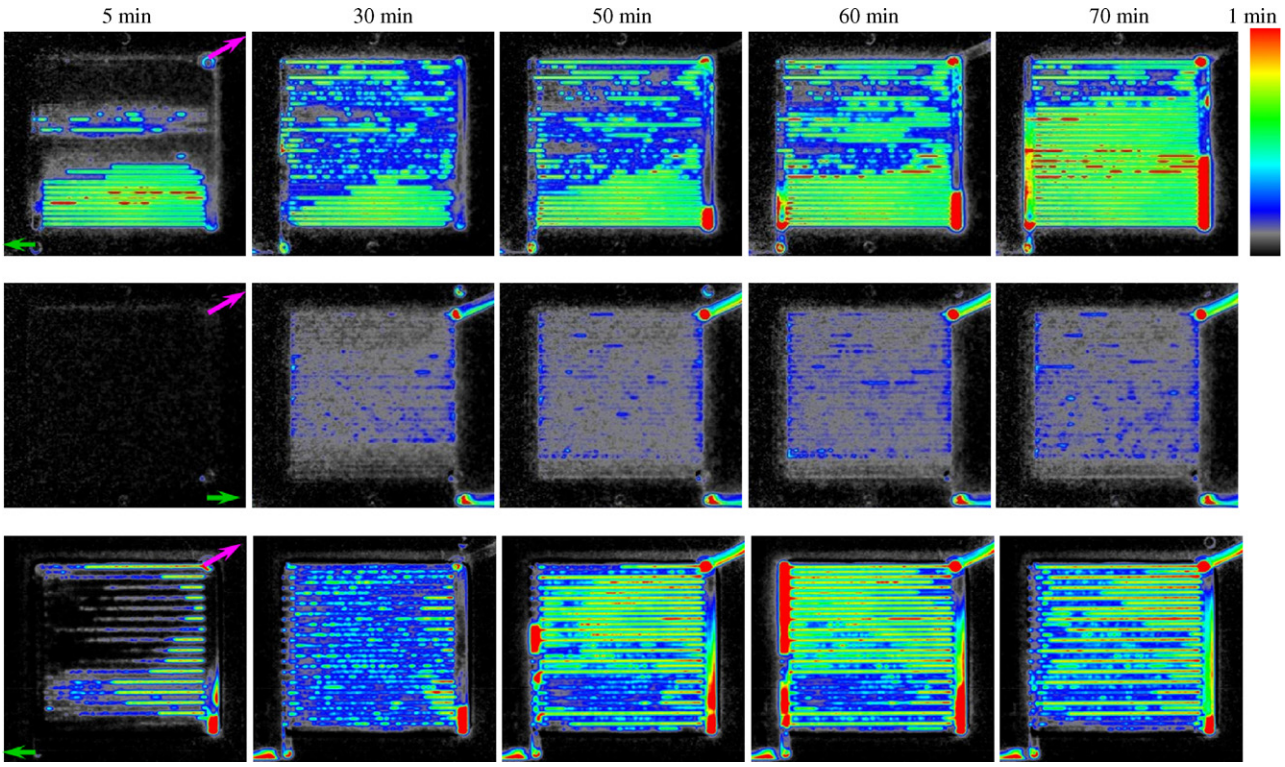

Fig. 5. Neutron images showing water distribution at different times while recording the polarization curves shown in Fig. 4. Top row: parallel, middle row: single-serpentine, bottom row: interdigitated flow field. Water thickness denoted by the color bar (range 0.01–1 mm). Same color scheme and thickness range used in all neutron images presented. Pink arrow: anode outlet; green arrow: cathode outlet. (For interpretation of the references to color in this figure legend, the reader is referred to the web version of the article.)

ily (i.e. until the benefit of the cathode relief becomes negated by the severe anode flooding). Water from the channels intermittently drains into the anode outlet because the hydrogen flow is not sufficiently strong to expel the water against the gravity. Hence, prolonged channel flooding spreads across the cell while the water keeps on collecting in the outlet (Fig. 5).

Next, the cell was tested after increasing the air flow rate from 1.5 to 5 slpm, while keeping everything else the same (Fig. 6). Similar trends in water content and dynamics were observed. Water initially accumulates at a high rate in the cathode channels, in the form of stationary growing droplets. Cathode pressure drop rises as the droplets increase in size and number, and reaches a maximum value once the droplets start merging into slugs (beyond 26 min). Anode pressure differential increases from then on. An initial, moderate increase (up to 40 min) due to the water buildup in the anode channels is followed by a steep rise from 40 to 60 min, mainly due to the outlet clogging by water drained from the channels.

Compared to the case with the lower air flow rate, cathode pressure differential is 7 times higher, whilst the limiting current almost doubles. While the positive Nernstian-type contribution and higher catalyst-site occupancy definitely enhance the performance, we note that the total amount of water stored in the cell does not differ as substantially between the two cases (the maximum value decreases by only 10–15% at higher cathode flow rate). To evaluate the water distributions, neutron and optical images from the two runs were compared for time instants when the overall water contents across the cell area were equal. The following observations could be made regarding the water distribution in the channels. First, water in both cathode and anode channels was distributed more uniformly when the air flow rate was higher. Second, water content in the cathode channels was slightly lower, while the similar values of the anode pressure differentials indicate that the water content in the anode channels was not substantially different. Thus, at higher current densities resulting from the increased air flow, saturation level of the GDL may be elevated. Additional analyses are needed to investigate to what extent the difference in the limiting currents was caused by the water distribution within the GDLs. Third, inactive cathode channels could be identified due to the fact that they contain short stationary slugs of water and do not show liquid water actively surfacing from the GDL. In the limiting current region, the number of such channels was reduced from 12 (low air flow rate) to 5 (high air flow rate). The stagnant slugs were identified by examining consecutive optical images of the cathode channels, and then confirming the locations of these stagnant pools of water to the areas in the neutron images that denote water thicknesses exceeding the channel depth. Clearly, this simple analysis can only account for a 20% increase in the effective active area due to the fewer blocked channels at higher flow rate.

In both cases discussed above, for the large part of the run, cell output does not react to the change in the overall water content but rather to fluctuations in the cathode pressure drop. These fluctuations in the pressure drop are caused mainly by formation of slugs (i.e. individual channel blockage) accompanied by the intermittent channel flushing. Thus, for the given operating conditions, the current density reacts to the liquid water distribution in the cathode channels. However, at water content above 900 mm^3, the cell output may respond instantaneously even to moderate variations in the water content. From the higher flow rate case (Fig. 6), the current density initially increases with the cell water content, and then shows a strong anti-correlation, primarily in response to the anode flooding throughout the second half of the test.

3.2.2. *Single-serpentine flow field*

Single-serpentine flow field (Fig. 4) reaches the limiting current density of 1.95 A cm^{-2} (the highest of all flow fields), while retaining the lowest water content (a maximum value of 325 mm^3).

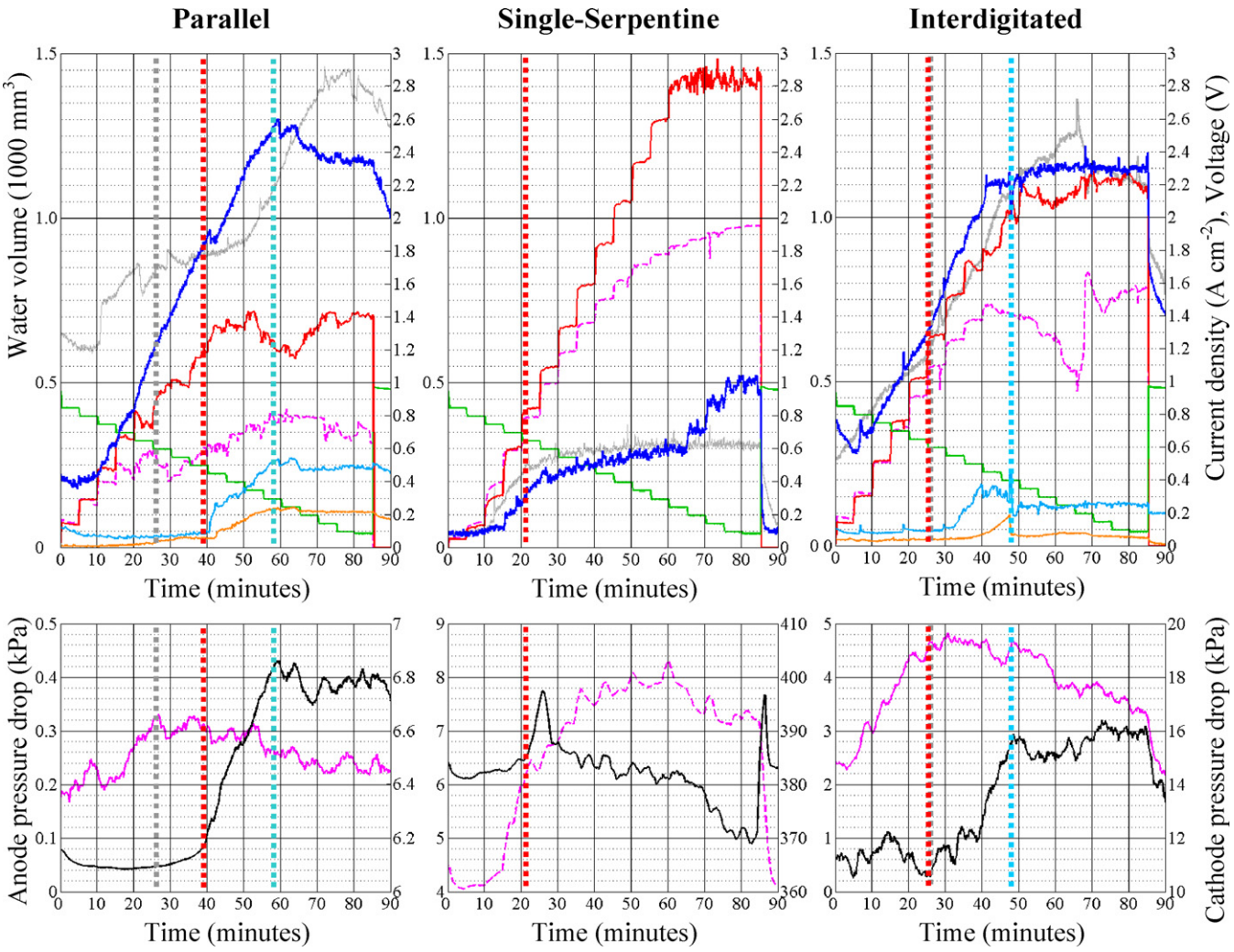

Fig. 6. Time evolution while recording polarization curves (Fig. 3) for the cell with visualized cathode channels, with air flow rate of 5 slpm. Legend shown in Fig. 4. Top: water content, current density and voltage vs. time. Data from Fig. 4 (1.5 slpm air flow) is re-plotted for comparison: water content over the cell active area (grey) and current density (pink, dashed). Bottom: pressure drop across anode and cathode sides of the cell vs. time. (For interpretation of the references to color in this figure legend, the reader is referred to the web version of the article.)

Owing to the high velocity of the gas streams, the vastly greater cumulative channel length, and the local pressure losses at U-turns, pressure differentials across the serpentine are two orders of magnitude higher than across the parallel flow field. Thus, the serpentine cell performance benefits both from the efficient water removal and the increased operating pressure. Large pressure gradients between the adjacent sections of the serpentine flow field induce the additional benefit of convective bypass under the lands.

It takes 10 min for liquid water to start surfacing at the GDL, as the serpentine cell enters the polarization sweep in a dry condition (the first image in Fig. 5) from the preceding purge. Having emerged at the GDL surface, droplets are almost instantaneously swept away by the air stream. Thus, in the period between 10 and 15 min, water is removed from the cathode channel via mist flow and in the form of very small droplets (less than 0.3 mm in diameter). Water accumulates at U-turns becoming evident after 15 min, while larger droplets and fast-moving films (as fast as 5 cm s^{-1}) appear across the cell area. Thus, the serpentine cathode channel exhibits highly dynamic water behavior, with frequent droplet-film interactions. Water removal is greatly enhanced by these interactions, which to some extent may explain a rather flat water content profile in spite of the increasing current density. This lack of increase in the water content beyond 50 min despite the rising current density may further be explained by the substantially smaller droplet-detachment diameter compared to the channel dimension.

Although the anode water does not show the highly dynamic movements as observed on the cathode side, active water removal from the anode channel is clearly evidenced by the water-filled anode outlet (Fig. 5, top-right corner in the neutron images). The occurrence of liquid water in the anode outlet at 1330 s coincides with the anode pressure differential reaching the maximum value of 7.3 kPa. From then on, water continues to depart the anode channel as a liquid (Fig. 5, 2nd to 5th image).

Increasing the air flow rate (Fig. 6) results in a lower overall water content in the first half of the test (250 vs. 300 mm^3 at 40 min into the test, Fig. 6). Optical images show that the level of the cathode-channel flooding is notably reduced throughout the test when compared to the first case. The size of droplets is notably smaller (it rarely exceeds 0.4 mm in diameter), while water is removed from the cathode channel mostly in the form of mist flow and fast-moving thin films. Water clusters at cathode U-turns are also reduced in size. It should be noted that the water movements in the channel are often too fast to be captured by optical recording at the frame rate of 2 Hz. Note that the cathode pressure drop (Fig. 6), recorded by the sensors in the test stand, is shown for

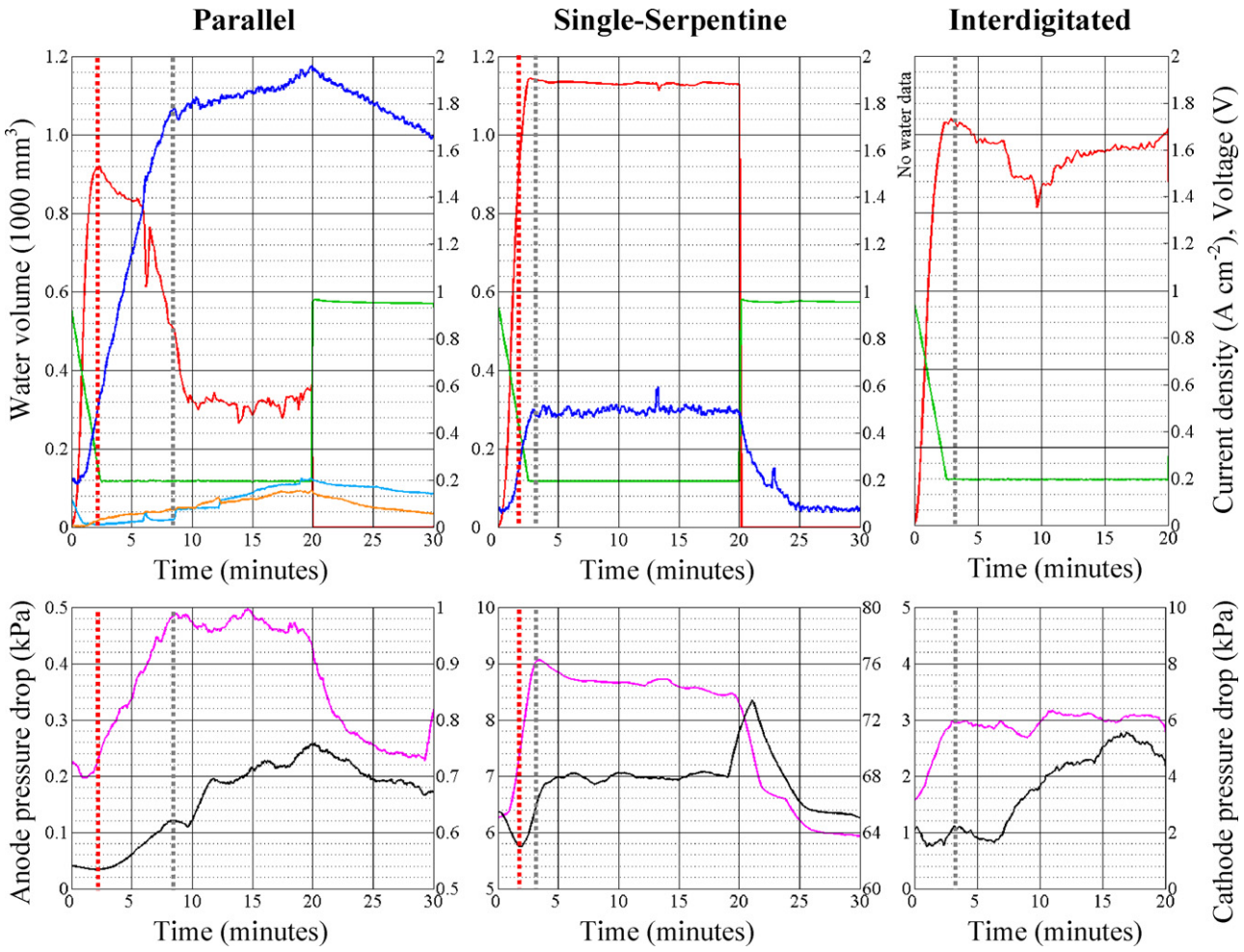

Fig. 7. Time evolution during the cell startup, at constant voltage 0.2 V, after switching from open circuit (1.5 slpm air flow rate). Legend shown in Fig. 4. Top: water content, current density and voltage vs. time. Bottom: pressure drop across anode and cathode sides of the cell vs. time.

qualitative purposes as it exceeds the 210 kPa range of the pressure sensor connected to the cell inlet and outlet.

On the anode side, liquid water removal starts around 1600 s, and again coincides with the peak in the pressure differential (7.7 kPa). When considering the pressure data presented, one should note that the flow rate on either side of the cell was held constant throughout the test. Thus, pressure differentials across the flow fields while recording the polarization curves respond to the competing effects of water accumulation in the cell and the increased gas consumption at higher current density. The overwhelming effect of the gas consumption is clearly visible in Fig. 6, where the serpentine anode pressure drop decreases with the current density, in spite of the notable anode flooding. Limiting current density, reached at 60 min, corresponds to complete hydrogen consumption. Consequently, the increase in the overall water content of 200 mm^3 during the last 20 min (from 285 to 485 mm^3) corresponds entirely to the anode flooding. Also taking into account that both anode and cathode gas streams are fully humidified, we reiterate the strong impact of the cathode microporous layer on water transport across the membrane (additionally aided by a very thin membrane).

Towards the end of the test, the downstream third of the anode flow field (top 12 channel passes) contains long continuous films of water, of thickness ranging from 0.5 to 0.8 mm. Despite almost half of the liquid water stored in the cell residing on the anode side, the above facts indicate that the anode flooding is not the current-limiting factor in the present case. While such a substantial amount of liquid water on the anode side did not show immediate significant impact on the serpentine cell performance, the influence of prolonged anode flooding on durability of the cell components requires further attention.

Finally, although high pressure differential across the serpentine channel ensures efficient removal of the excess water, it also represents a parasitic loss that should be taken into account when evaluating the balance of plant for the fuel cell system. Moreover, the MEA may suffer damage due to the large pressure difference between cathode and anode sides in the present cell design. Besides, increasing the cell area (or, the channel length) may lead to excessively large pressure drop across the flow field.

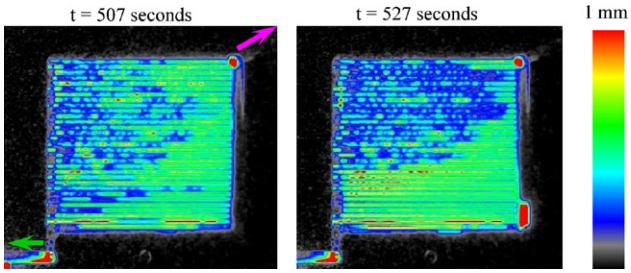

Fig. 8. Water redistribution in the anode channels of the parallel flow field during the cell startup (time evolution shown in Fig. 7). Pink arrow: anode outlet; green arrow: cathode outlet. (For interpretation of the references to color in this figure legend, the reader is referred to the web version of the article.)

3.2.3. Interdigitated flow field

In the *interdigitated flow field*, current density increases with the overall water content within the cell throughout the first half of the polarization sweep (Fig. 4). Having reached the value of 1.47 A cm^{-2} at 43 min, the current density shows anti-correlation with the water content during the remainder of the test (primarily due to anode flooding). It is worth noting that the performance of the interdigitated cell matches the serpentine over the first 40 min, but with three times more liquid water stored in the cell than the serpentine cell.

The first image in the sequence (5 min into the test, Fig. 5) shows mostly anode water in both channels and manifold (except for the sagging slug which is located in the cathode inlet). Similar to the situation encountered with the parallel cell, purging between the steps in the long test was not sufficient to remove all the water from the interdigitated channels. However, this residual water did not significantly affect the performance, since most of it was removed from the anode channels during the first 15 min after stepping up the current draw, aided by evaporation due to the increasing heat release. At the end of the initial 15-min period, water distribution on both sides is uniform across the cell area, with significantly higher flooding level on the cathode side, as expected.

Water accumulation on the cathode side undergoes two distinct stages. Continuous, steep water buildup is evidenced by the gradual increase in the cathode pressure differential over the first 30 min. The end of this phase is marked by the grey dotted line in Fig. 4. Thereafter, the cathode pressure drop retains a rather steady value (around 2.5 times higher than at the step start). Hence, water accumulation on the cathode side slows down drastically after the initial 30-min period.

Subsequently, water starts accumulating at a higher rate in the anode flow field. From 30 to 43 min, water accrues in the anode channels, and intermittently drains from the anode outlet channels into the outlet manifold (bottom right corner in the neutron images, Fig. 5). Current density continues to increase in this period, albeit with much smaller step heights. Active water removal from the anode side is evidenced by the wet anode outlet connection (top right corner in the neutron images, similar to the serpentine channel). The large cluster in the mid-region of the anode inlet (Fig. 5, 50 min) originated from almost concurrent clogging of three adjacent anode inlet channels. This event sets in motion further clogging of the anode inlet (see the manifold water content in Fig. 4), causing a severe decrease in the current density (by 36%). A spike in the pressure drop denotes the subsequent clearing of the anode flow field and the recovery of the cell output.

Operation at the higher air flow rate revealed the same trend as above: both the water content and current density increased during the first half of the sweep, while they were anti-correlated in the second half of the test. In contrast to the unstable output and variations as high as 0.6 A cm^{-2} seen above, the limiting current value of 2.2 A cm^{-2} is more clear-cut in the present case due to absence of complete manifold clogging. Pressure drop data indicates that the cathode again undergoes two stages of water buildup: fast accumulation in the first 30 min, followed by a more modest accumulation rate thereafter. Once the cathode pressure differential has reached the maximum value, water starts accumulating rapidly in the anode channels.

When compared to the run with 1.5 slpm of air (Figs. 4–6), several distinctions in the channel water dynamics and distribution were observed at higher flow rate. The cathode water removal is improved due to the increased flow rate and roughly 2.5 times higher pressure differential. Water in the cathode channels is divided into smaller, scattered droplets, compared to larger continuous clusters seen in the previous test. Moreover, the cathode shows less water in channels (confirmed via optical images). In summary, while the total water content within the cell is almost the same, increase in the limiting current density by 0.5 A cm^{-2} at higher flow rate resulted from Nernstian benefit and more uniform water distributions on both cathode and anode side.

3.2.4. General remarks on flooding

Presence of liquid water on both cathode and anode sides indicates that the overall hydration level of the membrane remained high in all runs regardless of the flow field, and that the excess water removal was among the key factors affecting the cell performance in the present tests. As the Bond number is almost an order of magnitude higher in the manifolds than in the channels, gravity aided the water removal from the cathode outlet manifold in both parallel and interdigitated flow field. In contrast, counter-gravity flow on the anode side promoted excessive clogging of the manifolds. Hence, critical levels of anode flooding strongly impeded the cell output. Although the imperfect manifold design and the influence of gravity and flow direction promoted the decrease in the cell output, it should be noted that severe anode channel flooding precedes the water accumulation in the manifolds. Anode channel flooding should therefore be expected regardless of the manifold design or cell orientation, and was present in all tests, be it with conventional or transparent cells. Finally, significantly lower *Re* on the anode side compared to the cathode side (Table 2) led to much slower water removal from the anode flow field.

3.3. Dynamic response during cell startup

Time evolution at the cell startup is presented in Fig. 7. The cells were operated at open circuit for 30 min before stepping down the voltage to 0.2 V. Since the flow rates were held constant at all times, pressure differentials initially decrease slightly in response to the sudden jump in the gas consumption, and increase immediately after as water starts accumulating in the cell.

When starting the cells from a dry state, first occurrence of droplets emerging from the cathode GDL surface took place in the period between 60 and 100 s, regardless of the flow field. This may be regarded as the characteristic time for capillary transport through the GDL. Capillary diffusion approximation may be used to model the water transport through the GDL [34–36]. The capillary diffusion coefficient will depend on the GDL material and the saturation level. One can estimate its value by using the characteristic time t ($\approx$80 s) and the thickness of the compressed GDL (L = 0.27 mm) as $D = L^2/t \approx 0.9 \times 10^{-5}$ cm^2 s^{-1} which agrees reasonably well with the values reported in previous neutron imaging studies [26] and suggested by modeling analyses [34]. As for the anode side, the onset of water accumulation in the channels does not lag behind that on the cathode side.

3.3.1. Parallel flow field

The *parallel* cell starts off with a steep increase in the current density (Fig. 7), reaching a peak of 1.53 A cm^{-2} at 140 s. However, the high initial liquid-water accumulation rate of 2.3 mm^3 s^{-1} causes the current density to decline sharply to 0.5 A cm^{-2} after 580 s. This illustrates the potential for high performance of the parallel flow field in the absence of excessive flooding. Performance of the parallel flow field would therefore greatly benefit from the improved water removal, be it via enhanced shear removal (e.g. by making the channels longer) or via evaporative removal (by reducing the relative humidity of the reactant gases).

Onset of droplet formation in the cathode channels occurs at 60 s after starting the fixed voltage step (coinciding with the dip in the cathode pressure differential), and is accompanied by fogging and condensation in the cathode outlet manifold. Within 200 s, the entire cathode flow field is populated with stationary droplets emerging from the GDL surface (with slightly less water coverage in the inlet portions of the channels). Around 350 s, large droplets

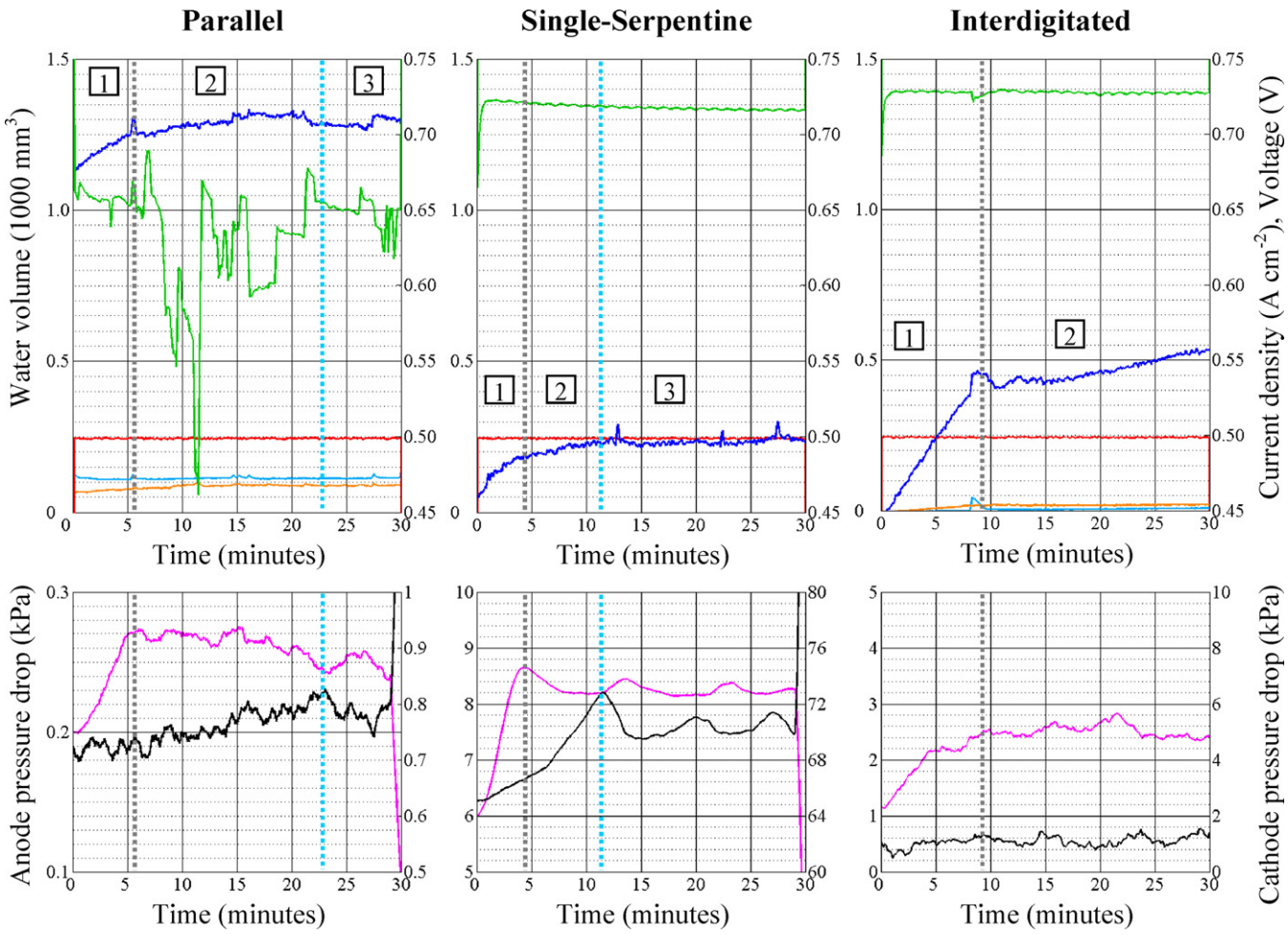

Fig. 9. Time evolution at constant current density 0.5 A cm^{-2}, after switching from open circuit (1.5 slpm air flow rate). Legend shown in Fig. 4. Top: water content, current density and voltage vs. time. Bottom: pressure drop across anode and cathode sides of the cell vs. time.

start to combine into short slugs (of several millimeters in length). This transition period is accompanied by a sharp decrease in the current density (350–500 s). While a certain amount of water in the channels is required for this transition to take place, we note that the slope of the total water content remains steady throughout the first 500 s, thus not showing any correlation with the discontinuity of the current-density slope. Similar to the situation presented in Fig. 6, the cell output responded to the change in the local liquid-water features in the channels, rather than to the overall water content within the cell.

Fig. 8 depicts neutron images before and after the redistribution of the anode channel water, wherein water from top anode channels drains into the outlet manifold. Such rearrangement of the anode channel water took place early in the testing cycle (within the first 10 min) every time the cell was restarted. This may help explain the image sequence in Fig. 5, in which the bottom portion of the cell contains more water due to a similar effect.

3.3.2. Single-serpentine flow field

Pressure differentials across the *single-serpentine* also exhibit local minima at the start, at 70 and 110 s for cathode and anode, respectively. Optical images of the cathode channel confirm that the first droplets surface at the GDL around 70 s. Water clusters at anode U-turns close to the exit are clearly visible after 180 s. The current density steeply increases and peaks at 1.9 A cm^{-2} at 150 s. In contrast to the parallel flow field, the serpentine cell continues to operate at steady value of 1.88 A cm^{-2} throughout the remainder of the fixed voltage step, while maintaining a low water content around 300 mm^3. At the end of the step (t = 20 min), a sudden rise in the hydrogen flow due to opening the electric circuit causes some of the discrete droplets located at U-turns to merge into slugs. These slugs instantaneously occupy a large portion of the channel cross-section, causing the spike in the pressure drop (also present in Figs. 4 and 6).

3.3.3. Interdigitated flow field

The *interdigitated* cell's current density peaks at 1.73 A cm^{-2} after 170 s. The current density declines below 1.4 A cm^{-2} within 10 min in response to the reduced effective area due to water accumulation. However, it does not show such a large overshoot as the parallel cell, although it is reasonable to expect the water content in the interdigitated channels to be substantial at high current. The cell continues to operate with fluctuations around 1.6 A cm^{-2}.

3.4. Cell response after stepping up the current density

Water content and dynamics were recorded after stepping up the current density (i) from zero to 0.5 A cm^{-2}, with 0.5 slpm of air (Fig. 9) and (ii) from zero to 1 A cm^{-2}, with 5 slpm of air (Fig. 10). Hence, the water production rates are held constant in these tests. Since the gas consumption is also constant, variations in pressure differentials on either side of the cell correspond to the changes in the water content and/or distribution.

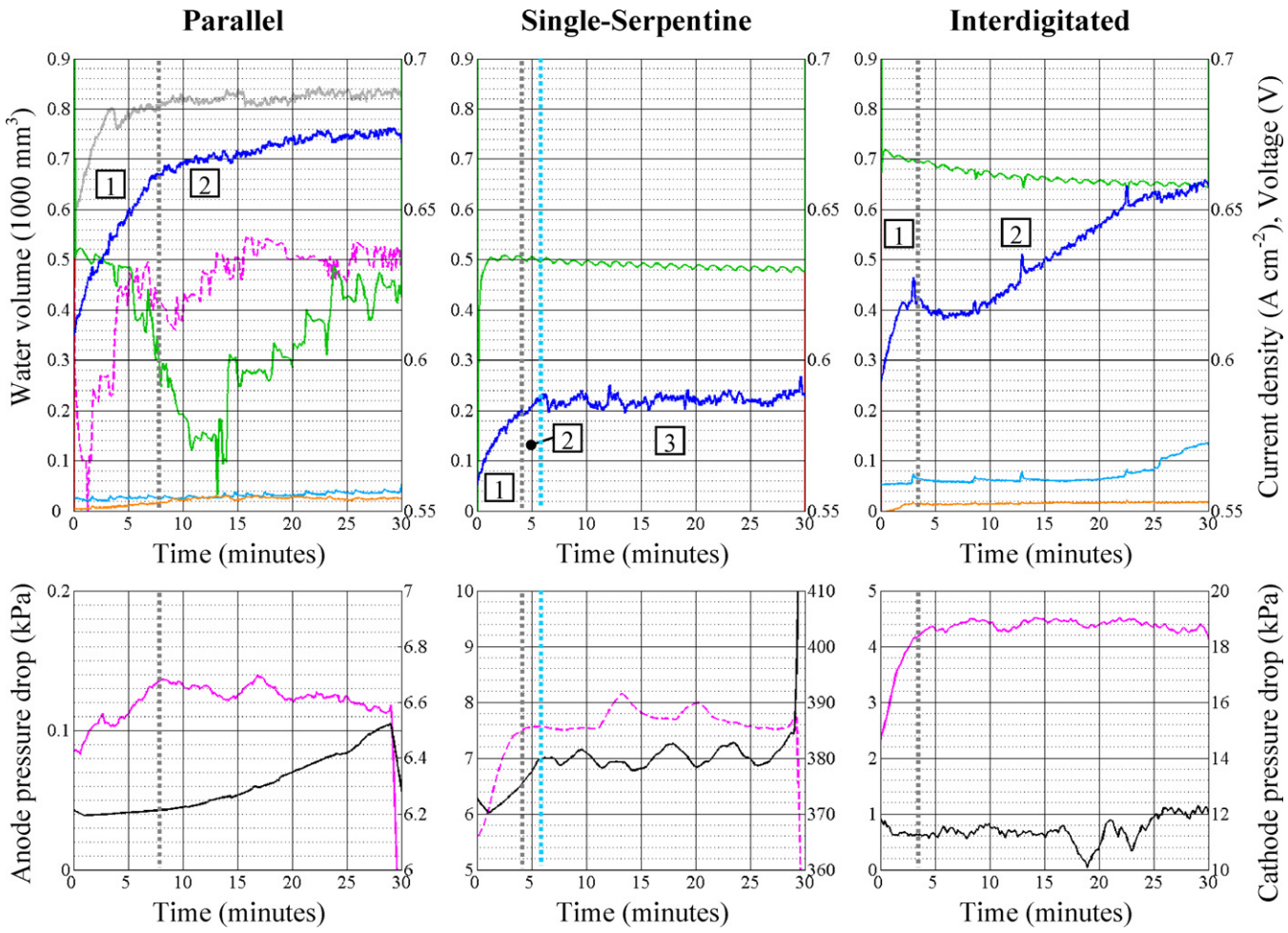

Fig. 10. Time evolution at constant current density 1 A cm^{-2}, after switching from open circuit (5 slpm air flow rate). Legend shown in Fig. 4. Top: water content, current density and voltage vs. time. Repeated run is shown in the top graph for the parallel channels (grey: water volume; dotted pink: voltage). Bottom: pressure drop across anode and cathode sides of the cell vs. time. (For interpretation of the references to color in this figure legend, the reader is referred to the web version of the article.)

3.4.1. Water content and accumulation rate

The water-content plot in Figs. 9 and 10 may be approximated as a piecewise linear function of time. Consequently, three distinct stages of water behavior (denoted in the graphs) could be identified as follows:

Stage 1 (steep slope): Both cathode and anode water content increase.
Stage 2 (moderate slope): Cathode water content approached steady state (water accumulation rate drastically decreases). Main features of water distribution as well as the liquid-water removal mechanisms on the cathode side are established.
Stage 3 (steady state): Water content on both cathode and anode sides fluctuates around steady-state values.

Liquid-water accumulation rates, obtained from Fig. 9 by linear fitting, are summarized in Table 3. The first stage exhibits the highest water accumulation rate (primarily on the cathode side) and is characterized by droplets surfacing at the GDL. In the single-serpentine, the droplets periodically re-emerge at the same preferential locations after being quickly swept away by the high-shear flow. In parallel and interdigitated flow fields the droplets continue to grow and populate the entire flow field (Fig. 11), occasionally combining into larger droplets.

Several important characteristics denote the transition from stage 1 to stage 2, common to all three flow field configurations:

1. Accumulation rate of liquid water in the cell changes significantly. This is indicated by the discontinuity in the slope of the total water-content evolution.
2. The transition coincides with the time instant when the pressure differential across the cathode side reaches the maximum value.
3. The main features of water distribution in the cathode channels are established: For the parallel and interdigitated cells, these are short slugs across the entire flow field. For the single-serpentine cell, these are water clusters at U-turns and films along the channel sidewalls.

While the above trend was common for all cells (Figs. 9 and 10), the duration of specific stage as well as the water content at which the cell shifts from one stage into another varied significantly with the flow field configuration. This 3-stage trend in the total water content after step-change in the current density is also in agreement with previous neutron imaging studies (e.g. Figs. 4, 5, and 8 in Ref. [26], and Fig. 3 in Ref. [28]). We note that the cells in these studies also had GDLs with MPLs, while employing different flow fields. In [26], it was speculated that the initial, steep portion of the water-content response corresponded to the GDL filling up with liquid water, whereas the subsequent lower water accumulation rate coincided with droplets accumulating in the flow channels. The present simultaneous imaging data provide additional insight that the rapid water accumulation during stage 1 is due to the combined con-

Table 3
Characteristic accumulation rates and water contents at fixed current density (Fig. 9) (water content includes the active area only, without the manifolds).

	Stage 1 ($mm^3\ s^{-1}$)	Water content at transition point (mm^3)	Stage 2 ($mm^3\ s^{-1}$)	Stage 3 = steady state (mm^3)
Parallel	>0.4	<1250	>0.1	1350
Single-serpentine	0.57	190	0.12	230
Interdigitated	0.86	420	0.13	>520

tribution of water accumulating in the GDL and in the flow fields.

The discontinuity in the water-content slope occurs at the transition between the first two stages, i.e. when the cathode's rate of water removal approached the rate of water accumulation. Stages 2 and 3 are characterized by active water transport in the cathode channels. Water removal is enhanced by frequent interactions between droplets, as illustrated in Fig. 12, where a large channel portion is cleared by the intermittent movement of a large droplet, merging with stationary droplets along the channel and spreading into film on the hydrophilic sidewalls.

3.4.2. *Liquid-water distributions in cathode and anode flow fields*

Water distribution in each flow field at the end of the test (Fig. 9) is shown in Figs. 13–15. Liquid-water distributions in the anode channels are also included, as the tests were repeated with the anode flow field visualized (without neutron imaging).

The *parallel* cathode channels show randomly distributed droplets and short slugs, while in the anode channels (Fig. 13d) liquid water is mainly concentrated in the downstream channel portion. The central area of the anode flow field exhibits periodic fogging and clearing throughout the test (with a period between 1 and 2 min). Fluctuating voltage response appears to be due to intermittent cathode channel blockage by the short slugs and subsequent purging (as illustrated in Fig. 12), additionally promoted by the clogging in the anode outlet.

In the *serpentine* channel (Fig. 14), anode water builds up exclusively in the U-turn regions. This water is rather stagnant, and is removed by occasional detachment of water clusters spreading onto the channel walls. Anode water is located only within the top 70% of the flow field, while the upstream portion of the channel shows no liquid water. Thus, the neutron footprint at U-turns comes from the combined contribution of water clusters on both cathode and anode side. Fast droplets and films in the cathode channel result in a smeared neutron signal over the entire cell area.

The *interdigitated* flow field shows uniform water distribution in the cathode channels during the first stage (Fig. 11). Over time, the upstream portions of the inlet channels get cleared, while the water remains accumulated towards the dead-end region of the channels (stagnation points, Fig. 15). The outlet channels contain droplets randomly distributed along the length, with pockets of stagnant liquid water at the channel origins. The interdigitated cell

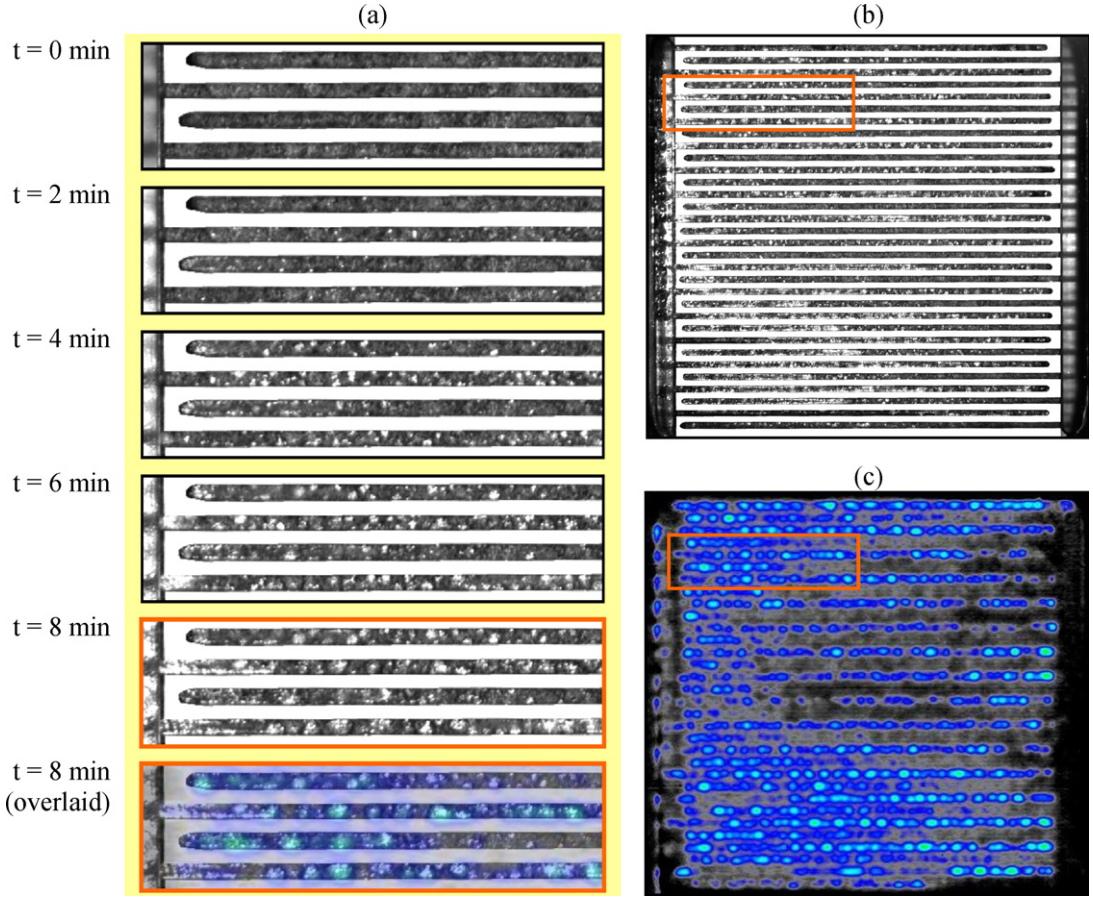

Fig. 11. Interdigitated flow field: water dynamics in the cathode channels during stage 1 (corresponding to the test data in Fig. 9). (a) Water accumulation in the cathode channels after stepping the current density from zero to 0.5 A cm^{-2}. Flow field portion shown is denoted by the rectangles in images (b) and (c). The bottom-most image shows the semi-transparent neutron image overlaid on top of the concurrent optical image, at t = 8 min. (b) Optical image of the cathode flow field at the end of stage 1 (t = 8 min). (c) Neutron image at the end of stage 1 (t = 8 min).

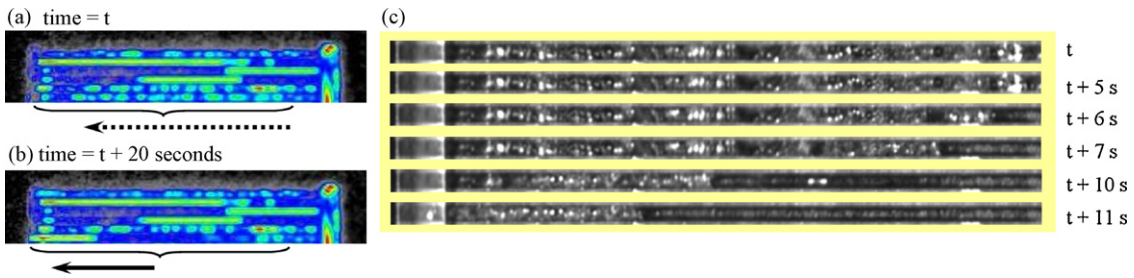

Fig. 12. Mechanism of water removal in the parallel cathode flow field: clearing a channel portion from stationary droplets triggered by a large moving droplet. (a) Neutron image at time = *t*: Stationary droplets occupying around 75% of the channel length. (b) Neutron image at time = *t* + 20 s: 50% of the channel length cleared by a moving water slug. (c) Optical images of the portion of the bottom channel shown in (a) and (b).

performed better than the serpentine, in spite of having 2–3 times more liquid water over the active area. However, the water content has not reached a steady value over the duration of the test, and impeding effects of flooding may still occur after prolonged operation.

Observations regarding the water dynamics in the *anode flow fields* may be summarized as follows. First, liquid water in the anode channels originated from condensation on the channel walls. In addition, very small droplets (on the order of 0.1 mm) were seen to appear in groups at the GDL surface. However, it cannot be concluded if these droplets arrived at the GDL surface via capillary flow (as they typically do on the cathode side), or they originated from condensation at the GDL surface. To conclusively determine if water is transported in a liquid form through the GDL into the anode channels, high-resolution techniques need to be employed, e.g. optical [12] or cross-sectional X-ray imaging [31]. Second, both the water accumulation rate and the overall water content are much lower than in the cathode flow field. Anode channel water dynamics, in general, appear like a slowed down version of the water dynamics in the cathode channels. It is interesting to note that in spite of the much less dynamic behavior, liquid water starts forming in the anode channels sooner than on the cathode side (more than twice as fast as on the cathode side). Further, water accumulation is limited to the downstream portion of the flow field.

Liquid water in the anode channels was not observed unless the cathode GDL had an MPL (several GDL materials were tested for comparison). Further, no water was observed while operating the cell at open circuit when the MPL was present, indicating that the anode water accumulation was derived from the water produced by the cell.

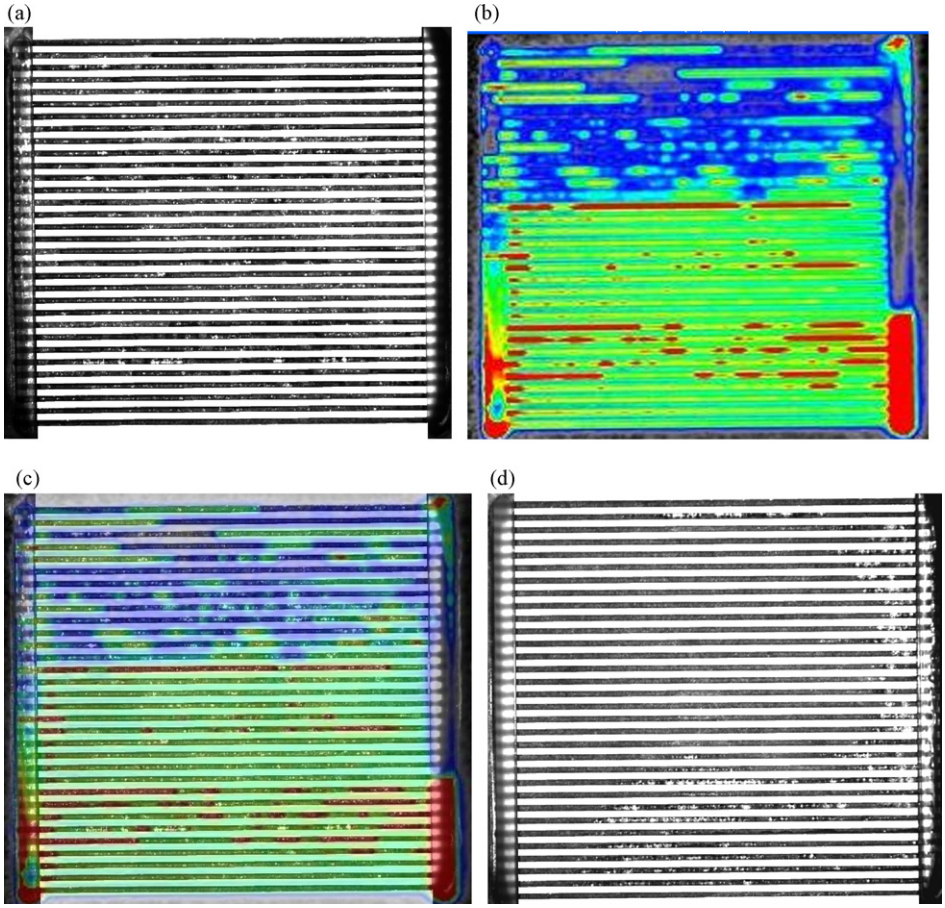

Fig. 13. Parallel flow field: water distribution at the end of the test step shown in Fig. 9. (a) Optical image of the wet cathode channels. (b) Concurrent neutron image. (c) Concurrent neutron image overlaid on top of the image (a). (d) Optical image of the wet anode channels (from the repeated run with visualized anode side).

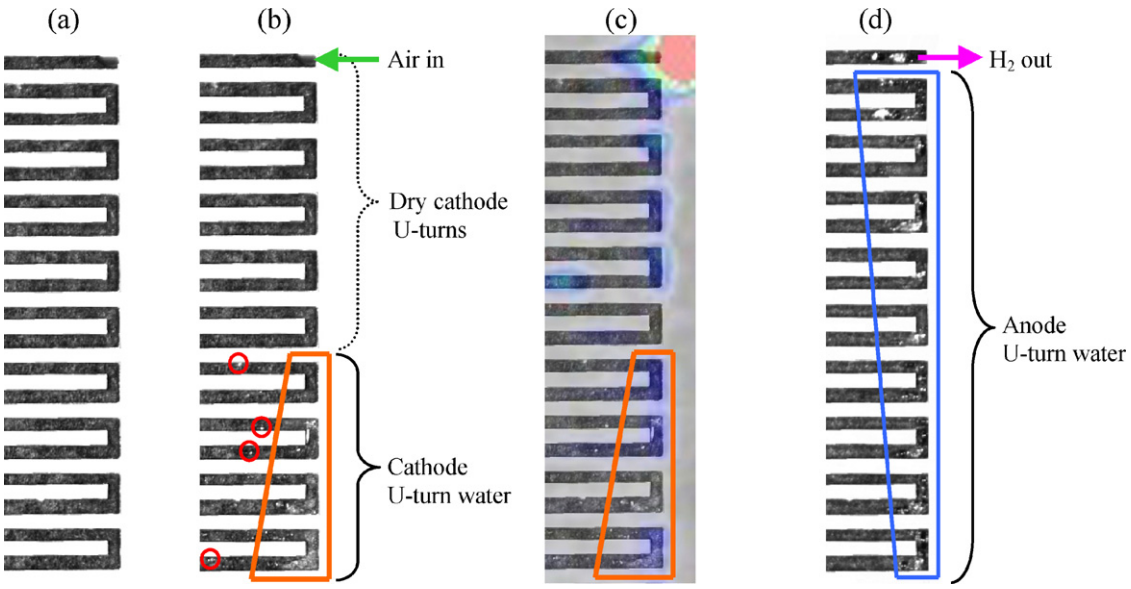

Fig. 14. Single-serpentine flow field: water distribution at the end of the test step shown in Fig. 9 (top right portion of the flow field shown). (a) Optical image of a dry cathode channel. (b) Optical image of the wet cathode channel (fast moving droplets circled in red). (c) Concurrent neutron image overlaid on top of the image (b). (d) Optical image of the wet anode channel (from the repeated run with visualized anode side). (For interpretation of the references to color in this figure legend, the reader is referred to the web version of the article.)

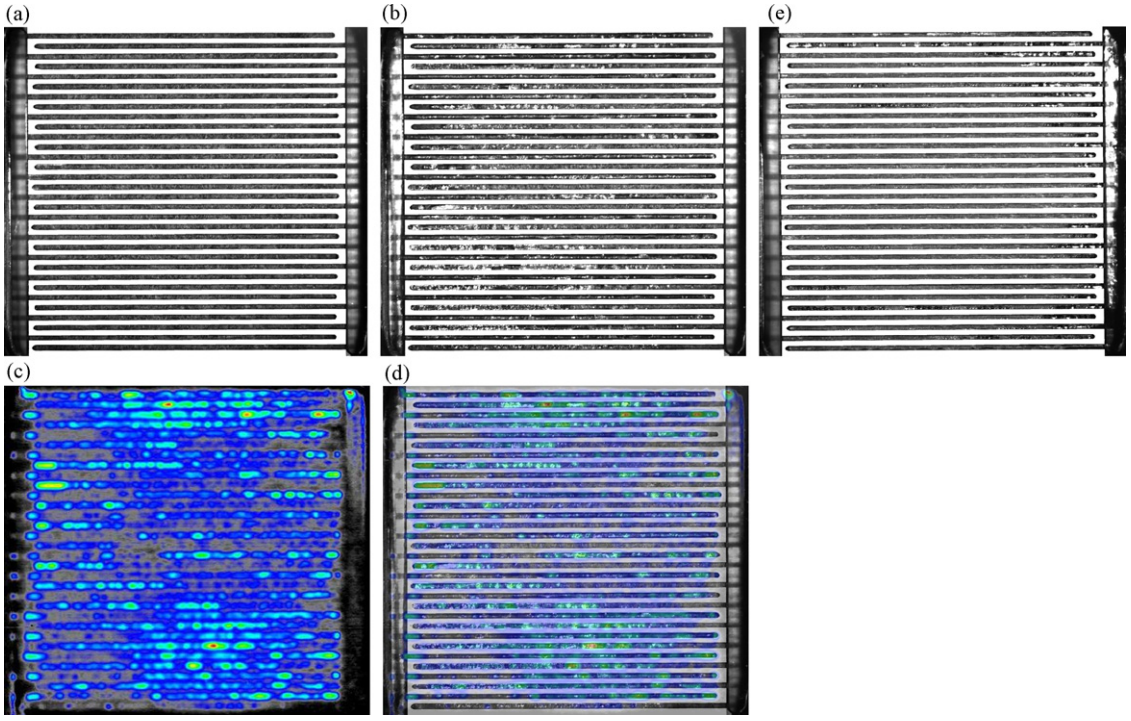

Fig. 15. Interdigitated flow field: water distribution at the end of the test step shown in Fig. 9. (a) Optical image of a dry cathode flow field. (b) Optical image of the wet cathode channels. (c) Concurrent neutron image. (d) Concurrent neutron image overlaid on top of the image (b). (e) Optical image of the wet anode channels (from the repeated run with visualized anode side).

4. Summary and conclusions

Liquid water formation, distribution and removal were recorded in operating PEM fuel cells via simultaneous neutron and optical imaging. Water dynamics were investigated and compared for three flow fields: parallel, single-serpentine, and interdigitated. Through-thickness integrated water content was measured across the cell via neutron imaging, whereas water dynamics in the flow-field channels were recorded optically with a digital camera.

The cell's water-content response to a step-change in current may be approximated by a piecewise linear function, revealing three stages of water evolution (regardless of the flow field). The first stage exhibits the highest water accumulation rate. The regime is characterized by discrete droplets surfacing at the GDL in the cathode channels. In the serpentine channel, droplets are swept away while still small, whereas in the parallel and interdigitated cell droplets increase in number and size while adhering to the GDL and channel sidewalls. It was demonstrated that the duration

of the first stage of water accumulation (a) depends strongly on the flow field design, and (b) exceeds the characteristic time for capillary transport of water through the GDL. Water accumulation rate reduces significantly in the second stage, as the main liquid-water removal mechanisms on the cathode side are established. The third stage is denoted by the flat overall water content profile, whereas cathode and anode side fluctuate around the steady-state values for both the water content and pressure differential.

The parallel flow field exhibits inferior performance and unstable operation even at modest current density, with the highest water content. Slow water removal is caused by the lowest channel velocity (Reynolds number) and pressure differential across the cell. At moderate current density, the cell output responds to the changes in water distribution in the cathode channels rather than to the changes in the total water content. These variations are caused by short slugs that block individual channels and are intermittently purged by interacting with moving droplets and channel walls. Such interactions are the main water removal mechanism in the parallel and interdigitated outlet channels. Operation at higher current is accompanied by severe flooding on both cathode and anode side, whereas the cell output anti-correlates with the changes in the total water content.

The single-serpentine cell yields stable output at all current densities, reaching the highest limiting current. The cell maintains the lowest water content (more than 4 times lower than the parallel cell) and a pressure differential that is almost two orders of magnitude higher than in parallel channels.

The interdigitated cell performs as well as the serpentine at most current densities, in spite of significantly higher water content in the cell. Hence, convective transport under the lands proved to be very beneficial for the cell performance, as it compensated for the adverse effect of substantial water content in the channels. Water tends to concentrate in the downstream portions of the inlet channels. In the outlet channels, water distribution and removal are very similar to the parallel channels.

Anode flooding occurred in each flow field, and was caused by the water transport across the membrane due to the microporous layer on the cathode GDL. Flooding of the anode channels was more pronounced at higher current. The main water-distribution features of the cathode flow field were replicated on the anode side. However, water originated from condensation rather than from capillary transport through the GDL as on the cathode. Cell performance with parallel and interdigitated flow fields was especially impeded by the excessive anode flooding at high current.

Acknowledgements

The authors gratefully acknowledge the assistance of NIST personnel, especially Dr. David Jacobson and Dr. Daniel Hussey, for their guidance while using the NIST Neutron Imaging Facility, as well as for the help with data processing. We also thank Mr. Darren Brown, Mr. Francesco Mazzocchi-Alemanni, and especially Mr. Amir Sedigh Haghighat, for their help with setting up the experiments and data processing.

Funding for this work was provided by the Federal Transit Administration, and Delaware Department of Natural Resources and Environmental Control. We also thank the University of Maryland Neutron Outreach Program for covering part of the travel costs for the neutron imaging experiments at NIST.

References

[1] D.J.L. Brett, N.P. Brandon, J. Fuel Cell Sci. Technol. 4 (2007) 29–44.
[2] B.D. Cunningham, J. Huang, D.G. Baird, Int. Mater. Rev. 52 (2007) 1–13.
[3] X.G. Li, M. Sabir, Int. J. Hydrogen Energy 30 (2005) 359–371.
[4] A.Z. Weber, R.M. Darling, J. Power Sources 168 (2007) 191–199.
[5] S. Litster, C.R. Buie, T. Fabian, J.K. Eaton, J.G. Santiago, J. Electrochem. Soc. 154 (2007) B1049–B1058.
[6] K. Scott, in: W. Vielstich, A. Lamm, H.A. Gasteiger (Eds.), Handbook of Fuel Cells: Fundamentals, Technology, and Applications, vol. 1, Wiley, Chichester, England, 2003, pp. 70–95.
[7] D.P. Wilkinson, O. Vanderleeden, in: W. Vielstich, A. Lamm, H.A. Gasteiger (Eds.), Handbook of Fuel Cells: Fundamentals, Technology, and Applications, vol. 3, Wiley, Chichester, England, 2003, pp. 316–324.
[8] T. Van Nguyen, W. He, in: W. Vielstich, A. Lamm, H.A. Gasteiger (Eds.), Handbook of Fuel Cells: Fundamentals, Technology, and Applications, vol. 3, Wiley, Chichester, England, 2003, pp. 325–336.
[9] A. Bazylak, Int. J. Hydrogen Energy 34 (2009) 3845–3857.
[10] J. St-Pierre, J. Electrochem. Soc. 154 (2007) B724–B731.
[11] X.G. Yang, F.Y. Zhang, A.L. Lubawy, C.Y. Wang, Electrochem. Solid State Lett. 7 (2004) A408–A411.
[12] F. Zhang, D. Spernjak, A.K. Prasad, S.G. Advani, J. Electrochem. Soc. 154 (2007) B1152–B1157.
[13] D. Spernjak, A.K. Prasad, S.G. Advani, J. Power Sources 170 (2007) 334–344.
[14] D. Spernjak, S.G. Advani, A.K. Prasad, J. Electrochem. Soc. 156 (2009) B109–B117.
[15] K. Tuber, D. Pocza, C. Hebling, J. Power Sources 124 (2003) 403–414.
[16] F.Y. Zhang, X.G. Yang, C.Y. Wang, J. Electrochem. Soc. 153 (2006) A225–A232.
[17] K.S. Chen, M.A. Hickner, D.R. Noble, Int. J. Energy Res. 29 (2005) 1113–1132.
[18] E.C. Kumbur, K.V. Sharp, M.M. Mench, J. Power Sources 161 (2006) 333–345.
[19] C.H. Schillberg, S.G. Kandlikar, ICNMM (2007).
[20] E. Shirani, S. Masoomi, J. Fuel Cell Sci. Technol. 5 (2008) 041008.
[21] X. Zhu, P.C. Sui, N. Djilali, J. Power Sources 172 (2007) 287–295.
[22] D. Kramer, J.B. Zhang, R. Shimoi, E. Lehmann, A. Wokaun, K. Shinohara, G.G. Scherer, Electrochim. Acta 50 (2005) 2603–2614.
[23] D.S. Hussey, D.L. Jacobson, M. Arif, P.R. Huffman, R.E. Williams, J.C. Cook, Nucl. Instrum. Methods A 542 (2005) 9–15.
[24] D.S. Hussey, D.L. Jacobson, M. Arif, J. Fuel Cell Sci. Technol., in press.
[25] A. Turhan, K. Heller, J.S. Brenizer, M.M. Mench, J. Power Sources 160 (2006) 1195–1203.
[26] M.A. Hickner, N.P. Siegel, K.S. Chen, D.N. McBrayer, D.S. Hussey, D.L. Jacobson, M. Arif, J. Electrochem. Soc. 153 (2006) A902–A908.
[27] T.A. Trabold, J.P. Owejan, D.L. Jacobson, M. Arif, P.R. Huffman, Int. J. Heat Mass Transf. 49 (2006) 4712–4720.
[28] J.P. Owejan, T.A. Trabold, D.L. Jacobson, D.R. Baker, D.S. Hussey, M. Arif, Int. J. Heat Mass Transf. 49 (2006) 4721–4731.
[29] J.B. Siegel, D.A. Mckay, A.G. Stefanopoulou, D.S. Hussey, D.L. Jacobson, J. Electrochem. Soc. 155 (2008) B1168–B1178.
[30] M.A. Hickner, N.P. Siegel, K.S. Chen, D.S. Hussey, D.L. Jacobson, M. Arif, J. Electrochem. Soc. 155 (2008) B427–B434.
[31] C. Hartnig, I. Manke, R. Kuhn, N. Kardjilov, J. Banhart, W. Lehnert, Appl. Phys. Lett. 92 (2008) 134106.
[32] J.P. Owejan, T.A. Trabold, D.L. Jacobson, M. Arif, S.G. Kandlikar, Int. J. Hydrogen Energy 32 (2007) 4489–4502.
[33] R. Satija, D.L. Jacobson, M. Arif, S.A. Werner, J. Power Sources 129 (2004) 238–245.
[34] S. Mazumder, J.V. Cole, J. Electrochem. Soc. 150 (2003) A1510–A1517.
[35] D. Natarajan, T. Van Nguyen, J. Electrochem. Soc. 148 (2001) A1324–A1335.
[36] Z.H. Wang, C.Y. Wang, K.S. Chen, J. Power Sources 94 (2001) 40–50.